HiSST: 2nd International Conference on
High-Speed Vehicle Science & Technology
11–15 September 2022, Bruges, Belgium

Disturbance Evolution in Roughness-induced Vortices under Re-entry Conditions

Friedrich Ulrich [1], *Christian Stemmer* [2]

Abstract

This study investigates a re-entry scenario of an Apollo-like space capsule with Direct Numerical Simulations (DNS). The simulation includes the chemical equilibrium gas model. Cross-flow-like vortices are induced through random distributed roughness patches on the capsule surface. Two different machine-learning methods are used to predict the maximum vorticity magnitude downstream of a random roughness patch. A large DNS database is formed for training and testing of the neural networks. In order to understand the influence of the vorticity magnitude on the transition process, local one-dimensional inviscid (LODI) relations are used to describe perturbations at the inflow. The disturbance evolution in the streamwise direction is analysed with a two dimensional Fourier transformation in time and space. The vorticity magnitudes of the cross-flow-like vortices and the wall-normal vortex-core positions influence the transition location.

Keywords: *roughness, hypersonic flow, hypersonic boundary layer, laminar-turbulent transition, Machine Learning*

Nomenclature

Latin

$A_{q,r}$ – Amplitude coefficients in the roughness patch
c – speed of sound [m/s]
E – Energy [J]
$g(x)$ – function to smooth transition
h – surface height of the roughness patch [m]
I – inclination angle [rad]
h_{max} – maximum roughness height [m]
N – number of grid points [-]
n – wavenumber [-]
R – specific gas constant [J/kg K]
u – streamwise velocity [m/s]
u' – streamwise velocity disturbance [m/s]
v – wall-normal velocity [m/s]
w – spanwise velocity [m/s]
p – pressure [Pa]
p' – pressure disturbance [Pa]
q – generic variable in the flow field
$Q_{m,n}$ – spatio-temporal Fourier transformed generic variable
t – time [s]
T – temperature [K]
T' – temperature disturbance [K]
y_{core} – wall-normal position of the vortex core [m]

Greek

ρ – density [kg/m^3]
ρ' – density disturbance [kg/m^3]
μ – viscosity [kg/m/s]
λ – heat conductivity [W/m/K]
λ_0 – fundamental wavelength
$\phi_{q,r}$ – phase coefficients in the roughness patch
ω_x – streamwise vorticity [1/s]

Subscripts

q – multiples of fundamental roughness wavenumber in x direction
r – multiples of fundamental roughness wavenumber in z direction
0 – base flow values

[1] *Chair of Aerodynamics and Fluid Mechanics, Technical University of Munich, Germany, fritz.ulrich@tum.de*
[2] *Chair of Aerodynamics and Fluid Mechanics, Technical University of Munich, Germany, Christian.Stemmer@tum.de*

1. Introduction

A Thermal Protection System (TPS) of a space capsule is able to withstand the extreme thermal stress which occurs due to the air friction of the high-speed vehicle in a re-entry scenario. A proper understanding of the re-entry aerodynamics of these blunt bodies is a mission critical aspect in order to improve the safety of a space mission. The heat-transfer rate can increase by one order of magnitude in case laminar to turbulent transition of the boundary layer occurs. However, a precise prediction of the laminar-turbulent transition is yet not possible and the physical mechanism is not fully understood in present literature. It is necessary to provide a base for future transition criteria by gaining a deeper understanding of the physical mechanism to provide a more reliable and safe spacecraft as well as to reduce cost and weight.

The investigation of roughness-induced transition relied heavily on experimental investigations due to the lack of computational resources. A summary of such experiments was described by Schneider [1]. Several DNS with different isolated roughness elements were investigated by Van den Eynde *et al.* [2]. A Mach 6 flow over a flat plate with a roughness element was computed. The study took several different factors of the roughness element into account, e.g. the shape and the planform of the roughness. Further, disturbance levels of the freestream were also considered. It was noted that a major effect on the transition process had not only the frontal, but also the aft section of the isolated roughness element. The detached shear layer at the ramped-down aft section of the roughness element was spread out and reduced in strength and led to a lower instability growth rate.
Di Giovanni and Stemmer [3] studied distributed roughness elements in a re-entry scenario of an Apollo-like space capsule. In the wake of the roughness, unsteady disturbances were amplified in cross-flow-type vortices. The highest amplification was observed in the vortices created by the highest skewed roughness peaks. The focus of the study was on the disturbance amplification for different chemical models (chemical equilibrium, chemical/thermal non-equilibrium). A destabilising effect of the chemical non-equilibrium occurred in the proposed set-up.
A roughness with a sinusoidal and triangular base function with the same maximum roughness height were compared by Ulrich and Stemmer [4]. This setup was chosen to better understand the role of the roughness geometry of distributed patches in terms of their vorticity generation. For patches with a triangular base-function, stronger streamwise vorticity was observed in the wake compared to sinusoidal ones. The growth of unsteady disturbances is analysed with a 2D Fourier transformation for both roughness types. The breakdown of the cross-flow-like vortex is observed for both sinusoidal and triangular roughness patches. For the triangular patch, transition is occurring further upstream, due to earlier disturbance amplification in the stronger wall-normal and spanwise gradients of the streamwise velocity.

Brunton *et al.* [5] give an overview of the usage of machine-learning (ML) methods in the field of computational fluid mechanics and emphasise its potential. Specifically on the influence of a rough distributed surface topology on turbulent flow, Jouybari *et al.* [6] introduce a Deep Neural Network (DNN) and Gaussian Process Regression (GPR) to predict the Nikuradse equivalent sand-grain height k_s. The ML based method performed significantly better compared to conventional polynomial models. An average prediction error of less then 10% was achieved for a database with different roughness types. Jouybari *et al.* hope to predict physics-related flow quantities, e.g. flow separation locations, with their approach in the future.

This study investigates the influence of different streamwise vorticity magnitudes on the laminar transition process. It compares two different data-driven machine-learning methods (*Deep Neural Networks* and *Convolutional Neural Networks*(CNN)) for the prediction of the streamwise vorticity magnitude. For training, validation and testing of the networks, a DNS database is formed with 9180 simulations of a reduced domain containing a random distributed roughness patch. In the second part of the study the unsteady downstream disturbance evolution is investigated for the different vorticity magnitudes with a 2D Fourier transformation.

2. Governing Equations

The investigation uses the compressible Navier-Stokes-Equations to perform Direct Numerical Simulations.

$$\frac{\partial \rho}{\partial t} + \frac{\partial}{\partial x_i}\left(\rho u_i\right) = 0, \tag{1}$$

with the density ρ and the velocity component u in the Einstein summation notation. Further, we use the following momentum equations:

$$\frac{\partial}{\partial t}\left(\rho u_i\right) + \frac{\partial}{\partial x_j}\left(\rho u_i u_j\right) = -\frac{\partial p}{\partial x_i} + \frac{\partial \sigma_{ij}}{\partial x_j}, \tag{2}$$

with the spatial coordinates x_i and the time t. The stress tensor σ_{ij} is computed with the viscosity μ and

$$\sigma_{ij} = \mu\left[\left(\frac{\partial u_i}{\partial x_j} - \frac{\partial u_j}{\partial x_i}\right) - \frac{2}{3}\frac{\partial u_k}{\partial x_k}\right]. \tag{3}$$

The energy equation is defined the following way,

$$\frac{\partial \rho E}{\partial t} + \frac{\partial}{\partial x_j}\left[\left(\rho E + p\right) u_j\right] = \frac{\partial}{\partial x_j}\left(\sigma_{ij} u_j\right) + \frac{\partial}{\partial x_j}\left(\lambda \frac{\partial T}{\partial x_j}\right), \tag{4}$$

For the chemical modeling, Park's two temperature model [7] is used. It uses five different species (N_2, O_2, NO, N, O). In this model, the equilibrium constants for the chemical equations are obtained by polynomials. Additionally, the single-species viscosity is computed by Blottner's formula [8]. Hirschfelder *et al.* [9] describe the single-species thermal conductivity. All single-species thermodynamic properties are combined with Wilke's mixing rule [10].

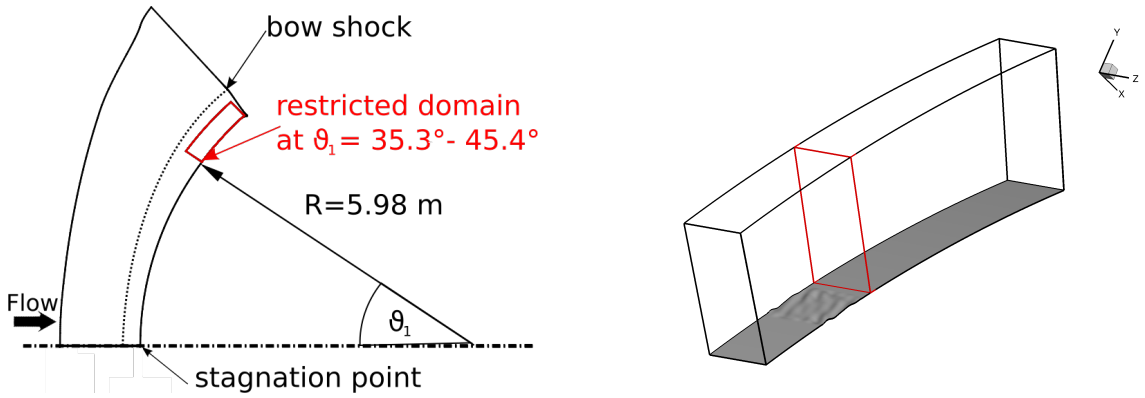

(a) Full domain (b) Reduced/restricted domain

Fig 1. Sketch of the full (a), restricted and reduced restricted (b) domain.

3. Numerical set-up

A semi-commercial finite volume solver called Navier Stokes Multi-Block Solver (NSMB) is used in this investigation. It utilizes the Message-Passing-Interface (MPI) to work in parallel by communicating data between different blocks. The computations were performed on the SuperMUC HPC System at the high performance computing facility of the Leibniz Rechenzentrum (LRZ) in Garching b. Munich. It was used and validated in previous hypersonic studies, e.g. [11].

The DNS performed in this study are done in three steps. At first, a two dimensional simulation for the entire capsule is computed which provides the necessary inflow conditions for the three dimensional

simulations. This preliminary simulation is conducted on a two axisymmetric dimensional grid (see Fig. 1a). In a second restricted domain (Fig. 1b), a three dimensional steady simulation is performed based on the conditions computed in the 2D simulation. For the unsteady simulations, the domain is further reduced and only the wake flow of the roughness (downstream of the red rectangle in Fig. 1b) is observed. Previous investigations [3] have shown that the main interaction between the disturbances and the vortical structures is happening in the wake flow of the roughness rather than with the roughness itself.

The 2D simulation is performed on a grid with about 80,000 grid points. The bow shock, which forms in front of the capsule's heat shield, is captured by an upstream splitting method (AUSM+) upwind scheme of first order accuracy. An implicit Euler time integration method is used to perform the study simulation. The restricted 3D domain has a size of 51.2 Million grid points and its grid resolution has been verified in previous studies [3, 11]. A fourth order accurate central scheme is chosen for the spatial discretization. A hybrid explicit Runge-Kutta Method is applied in the unsteady case.

The DNS database for the AI vorticity prediction is performed on a reduced domain which contains a random roughness patch, but has a shorter streamwise extension downstream of the patch, see Fig. 2. This reduction was necessary to be able to simulate a wide range of random roughness patches and focus on the vorticity production by the roughness patch.

The domain is 17 cm wide in the spanwise direction and has a streamwise extension of 28 cm. Also the maximum domain height is reduced to 6.6 cm compared to the restricted domain in Fig. 1b. The grid resolution is reduced to i=85 (streamwise direction), j=69 (wall-normal direction) k = 200 (spanwise direction). The resolution of the domain with a total number of grid points of 1,173,000 was tested by a grid convergence study. The maximum of streamwise vorticity downstream of the roughness patch was not affected by the chosen grid resolution for the reduced domain compared to the higher resolution of the restricted domain. The number of grid points in the wall-normal and spanwise direction were chosen to fully resolve the boundary-layer and the cross-flow-like vortex.

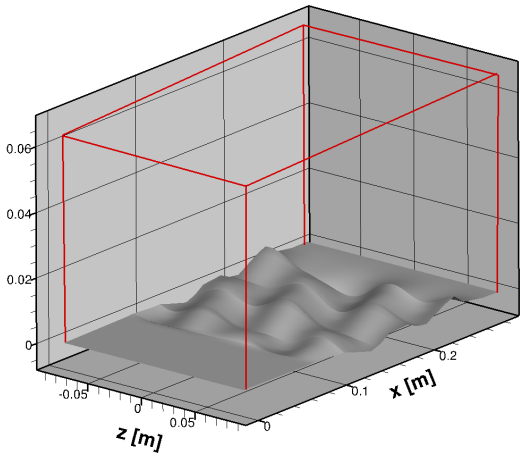

Fig 2. Reduced domain for the ML training and test database

4. Roughness generation

The roughness generation process used in this study was introduced by Di Giovanni and Stemmer [11]. It produces a pseudo-random distributed roughness pattern which is composed of several sinusoidal waves with different amplitudes and phases. The roughness height h relative to the wall surface is defined by

$$h(x,z) = h_{max} \cdot g(x) \sum_{q,r=1}^{3} A_{q,r} sin\left(\frac{2\pi q}{\lambda_0}x + \frac{2\pi r}{\lambda_0}z + \phi_{q,r}\right). \quad (5)$$

The function g(x) provides a smooth transition from the smooth wall to the roughness patch. The spanwise extension of the domain defines the fundamental wavelength λ_0. At the roughness location, the fundamental wavelength is λ_0=170 mm. The amplitudes $A_{q,r}$ and phases $\phi_{q,r}$ are defined in a random fashion. The amplitudes $A_{q,r}$ are set to zero for $q^2 + r^2 > 3^2 + 1$. This ensures that λ_0 is the minimum wavelength in all directions.
Equation 5 is used to generate a database of DNS with random distributed roughness patches. Every patch within the database has the same maximum height h_{max}=4.3 mm for better comparison.

4.1. Perturbation Generation

The steady cross-flow-like vortices in the wake of the roughness patch are perturbed with high-frequency perturbations in order to trigger transition. These waves are introduced at the inflow of the reduced domain. For modelling of these perturbations some assumptions are made: The perturbation amplitude is smaller by orders of magnitude compared to the base flow variables. The ratio between the disturbance pressure and the steady flow pressure is $p_{diss}/p_0 = 1 \cdot 10^{-6}$ at the boundary-layer thickness. Hence, the effect on the physical and chemical properties is minor. The properties are modelled as local one-dimensional inviscid (LODI) relations. The physical properties of the flow are locally constant for a certain height and are not changed by the small perturbations, but are changing in the wall-normal direction within the boundary layer of the base flow. This investigation is using a pressure, temperature, streamwise velocity u and density wave. The v- and w-velocity components are not included.
This considerations lead to the following wall-normal pressure function for a given time t at the wall-normal distance y

$$p'(y,t) = e^{-(y/\delta)} p_{diss}\, cos(2\pi f_{diss} t). \tag{6}$$

The disturbance frequency is $f_{diss} = 8.3$ kHz. This frequency showed disturbance growth in the wake for similar roughness configurations at a Mach 20 re-entry scenario in previous studies [4]. The pressure disturbance is damped outside the boundary layer with $e^{-(y/\delta)}$. Following the LODI procedure described in [12], the velocity perturbation is computed according to

$$u'(y,t) = \frac{1}{\rho_0(y) c_0(y)} p'(y,t), \tag{7}$$

and the temperature disturbance

$$T'(y,t) = \frac{T_0(y)}{\rho_0(y) c_0(y)^2} \left(\frac{c_0(y)^2}{R_0(y) T_0(y)} - 1 \right) p'(y,t), \tag{8}$$

with the variables $\rho_0(y)$, $c_0(y)$, $T_0(y)$ and $R_0(y)$ from the steady flow. Finally, the equation of state delivers the density perturbation,

$$\rho'(y,t) = \frac{p(y,t)'}{R_0(y) T'(y,t)}. \tag{9}$$

5. Machine-Learning Methods

In order to predict the maximum streamwise vorticity downstream of the roughness patch two different machine learning methods are tested: A Deep Neural Network and Convolutional Neural Network. The DNN is using geometric parameters derived from the roughness surface as input, the CNN is directly getting an image of the roughness surface as a input. Both networks are predicting the maximum streamwise vorticity downstream the roughness patch and are trained, tested and validated with simulations from the DNS database.

5.1. Deep Neural Network Setup

The Deep Neural Network is using a selection geometric parameters to compute the maximum vorticity at x=0.27 m downstream of the roughness patch. At first, the streamwise position of the highest peak $Pos_{max,i}$ and the lowest peak $Pos_{min,i}$ as well as the spanwise coordinates ($Pos_{max,j}$,$Pos_{min,k}$) are

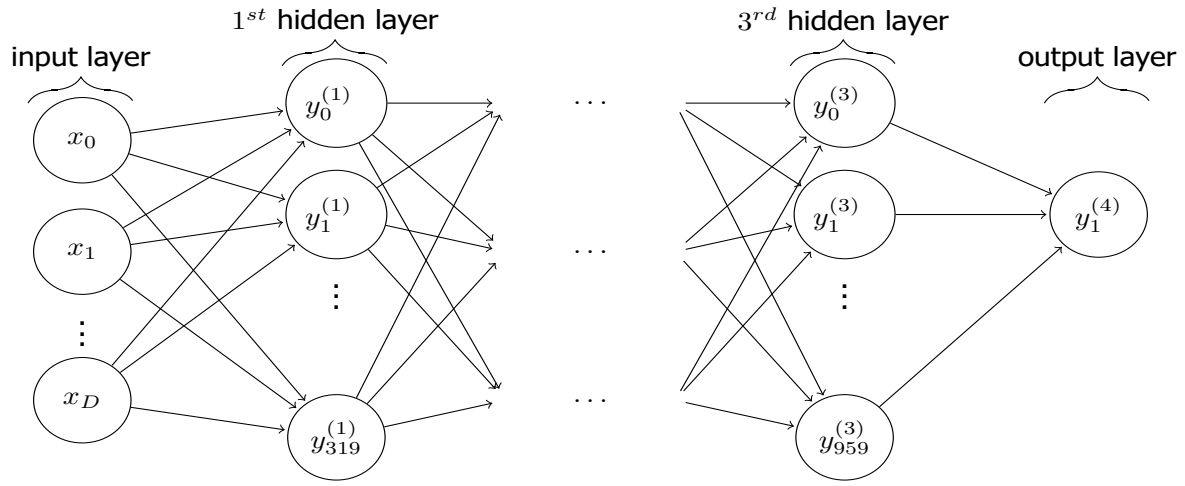

Fig 3. Network graph of the used DNN

included, because the vortex is generally formed downstream the highest peak and its adjacent valley. An initial study has shown that his factor has a significant influence on the prediction capability of the DNN.

Further, we used statistical functions to compute a single input parameter from a field of geometric values. These geometric features were the roughness height h(i,k), the streamwise derivative of the roughness heights

$$\frac{\partial h(i,k)}{\partial i}, \tag{10}$$

and the spanwise derivative,

$$\frac{\partial h(i,k)}{\partial k}. \tag{11}$$

Curvature values, such as the mean or Gaussian curvature did not significantly improve the prediction and hence were omitted from the database.

Then we computed the geometric average for the roughness height h_{avg},

$$h_{avg} = \frac{1}{N_i \cdot N_k} \sum_{i,k} h(i,k), \tag{12}$$

with the number of points N_i, N_k in the streamwise and spanwise directions, respectively.

The root-mean square (RMS) of the height is calculated as,

$$h_{rms} = \sqrt{\frac{1}{N_i \cdot N_k} \sum_{i,k} \left(h(i,k) - h_{avg}\right)^2}. \tag{13}$$

The skewness of the height values is defined as,

$$Sk(h) = \frac{1}{h_{rms}^3} \left(\frac{1}{N_i \cdot N_k} \sum_{i,k} \left(h(i,k) - h_{avg}\right)^3 \right). \tag{14}$$

The statistical functions used in Equations 12, 13 and 14 are applied to the spatial derivatives (Eq. 10,11) accordingly.

We derive the streamwise inclination angle from the skewness value of the streamwise derivative,

$$I_i = tan^{-1} \left(0.5 \cdot Sk \left(\frac{\partial h(i,k)}{\partial i} \right) \right), \tag{15}$$

and accordingly in the spanwise direction,

$$I_k = tan^{-1}\left(0.5 \cdot Sk\left(\frac{\partial h(i,k)}{\partial k}\right)\right). \tag{16}$$

For the training step, the data is split into training data (80%) and test data (20%). In both datasets, the input parameters are normalised before they are introduced to the network. The DNN is a multilayer perceptron *(MLP)* with three hidden layers. In this study, we used a DNN with 320 neurons in the first, 760 neurons in the second and 960 neurons in the third hidden layer. These dimension were determined by a hyperparameter study. The data is fed forward through the network by the *Exponential Linear Unit* activation function. Finally, the maximum streamwise vorticity is derived at the output layer as a single variable output. The structure of this network is visualised in Fig. 3.

5.2. Convolutional Network Setup

For the CNN, no input parameters are mathematically derived from the roughness patch. An image of the patch with the normalised roughness height as grey scale values is used as an input for this network. No further pre-processing of the data is necessary. The image has a resolution of 16×16 Pixel. A sample input image can be seen in Fig. 4 marked as input image. In this image, the height values are normalised from -1 (white) to 1 (black).

The network contains three convolutional layers with a filter size of 3×3. The rectified linear activation

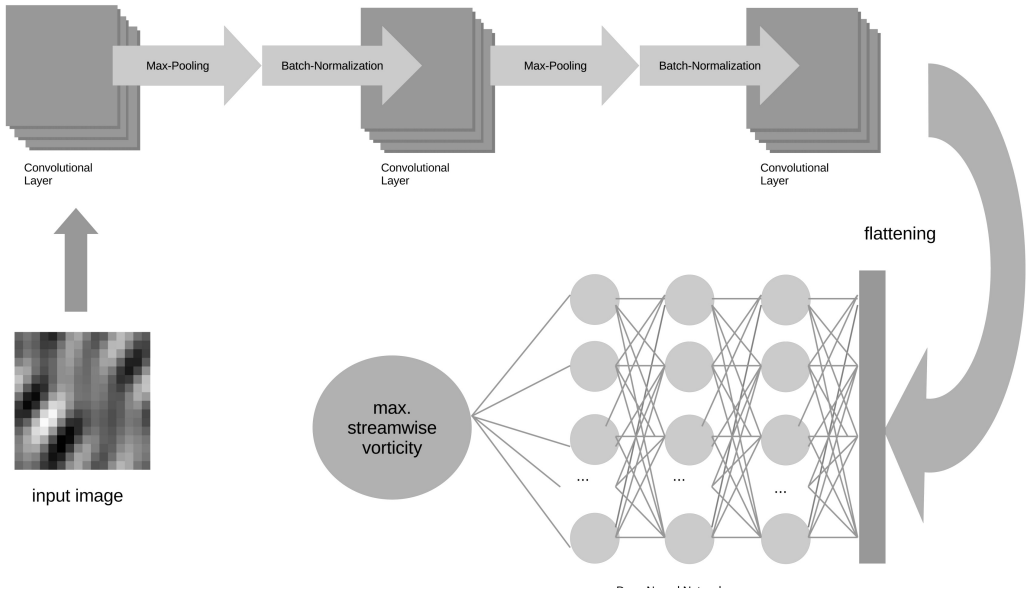

Fig 4. Structure of CNN

function (ReLU) is used. After each convolutional layer, a max pooling layer of the size 2×2 is added and the data is fed though a dropout layer. The 2D output of the CNN is flattened into a 1D array and sent through a DNN with three hidden layers to compute a single variable output. In total, the CNN has over 770,021 trainable features.

6. Results

This study investigates a Mach 20 re-entry flow at a flight altitude of about 57.5 km. The freestream conditions p_∞ = 29.9 Pa, T_∞=253.3 K, T_{wall}=1800 K and Re_∞= 1.97 · 10^6 m^{-1} are taken from an Apollo trajectory.

The main focus of this study is to investigate the influence of distributed roughness patches on the

disturbance evolution. Further, the prediction capability of the streamwise vorticity by machine learning methods is discussed.
At first, cross-flow-like vortices are observed in the steady wake flow of a distributed roughness patch. Fig. 5 shows a sample streamline through the vortex core with the strongest streamwise vorticity. The flow is passing over the distributed roughness patch. A temperature contour of a cross-section (x=0.27 m) in the wake is also displayed in Fig. 5. The strongest vortex emerges downstream the highest peak within the patch. This elevation in the patches forces fluid in the wall-normal direction. A vortical motion is induced in combination with the adjacent valley. It is observed, that the vortex is damped along the streamwise direction due to the strong acceleration in the flow (not shown). Further, the cross-flow-like vortex transports low-temperature fluid in higher regions of the boundary layer.
In the next sections, the capability of machine-learning methods to predict the maximum streamwise

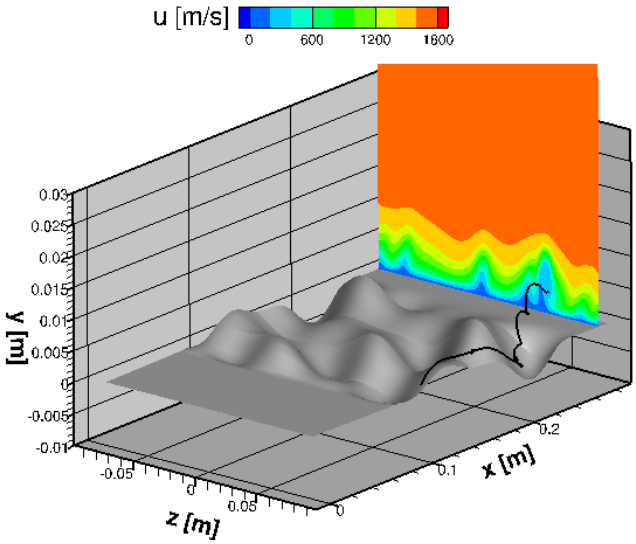

Fig 5. Detail restricted with random roughness and sample streamlines with temperature contour at x=0.27 m.

vorticity observed in the y-z-slice at x=0.27 m (see Fig. 5) is discussed. Further, unsteady simulations investigate the disturbance development in the wake.

6.1. Vorticity Prediction by the DNN and the CNN

The DNN was trained with a set of input parameters derived from the roughness surface, while the CNN was directly trained on the raw surface data. The training process for the CNN took twice as long compared to the DNN. However, both calculations were performed on a PC with only two CPUs in under 10 minutes and therefore are absolutely negligible compared to the computational effort the DNS database. The prediction capability of both methods is shown in Fig. 6. Here, the predicted data is plotted against the true vorticity values computed by the DNS. A perfect prediction is marked by the red line. Values above have a prediction which is too high and too low for simulations below the red line.

The CNN is predicting the vorticity with a mean error of 13.29% compared to the 17.36% of the DNN. The DNN can predict 90% of the test simulations within -3.5 $\cdot 10^4$ [1/s] - 4.5$\cdot$ 10^4 [1/s]. This confidence interval is marked by the blue and green line in Fig. 6. This margin corresponds to a prediction error below 35%. Further, the DNN methods computes 40% of the test set with an error below 10%. For only 4% of the values, the DNN prediction amounts to more than twice as much as the DNS vorticity value.
On the other side, the CNN is computing half of the vorticity value with an error below 10% and 90%

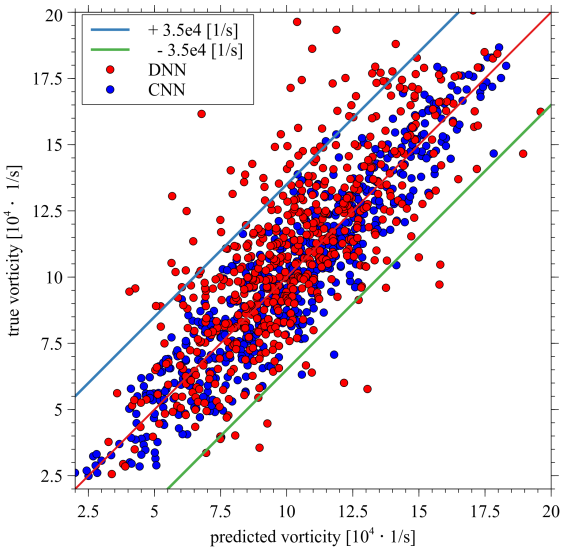

Fig 6. Comparison between predicted an simulated data for DNN (red) and CNN (blue)

of the data below 25%. Except for three simulations in Fig. 6, all DNN predictions (blue) are in the confidence interval. The error of the CNN is also smaller depending on the actual vorticity values. The DNN is weaker in predicting the correct value for very low or very small vorticity values, because there are less examples within the database. A summary of the different error quantities for both ML methods is summarised in Tab. 1.

A study with an increased input image resolution (32×32) did show improvements in the prediction

Table 1. prediction errors for the DNN and CNN

Error type	DNN	CNN
average error [%]	17.36	13.29
max. error [%]	152.27	90.21

capability. The relevant feature can be extracted from the input image with a resolutions (16×16) as long as notable roughness features, such as the maximum height in the patch, is sufficiently resolved. Hence, for patches composed with more sinusoidal waves a higher resolution might be necessary.
With a hyperparameter study, the DNN is able to reveal influential parameters for the prediction process and allow to a certain extent physical insight. The vortex formation is mostly influenced by the surface gradients of the roughness patch and the location of the highest peak and lowest valley within the patch. On the other hand, the CNN performs better in the vorticity prediction, but remains a black box.

6.2. Unsteady Simulations

The study investigates the effect of different streamwise vorticity magnitudes induced by three different roughness patches on the streamwise development (according to Eq. 18) of the unsteady disturbances. The streamwise velocity component is Fourier transformed in space and time and the amplitude development is described in this investigation.

The maximum streamwise vorticity ω_x for three different random roughness patches is provided in Tab. 2. The patches are chosen from the ML database and represent the lower third, the average and the upper third of the produced vorticity values within the database.
The introduction of unsteady disturbances at the inflow of the domain is destabilising the steady cross-flow-like vortex. The disturbances are amplified in the regions with large spanwise and wall-normal gradients in the shear-flow of the vortex. An iso-contour of the Q-criterion $Q = 5.5 \cdot 10^7$ shows the

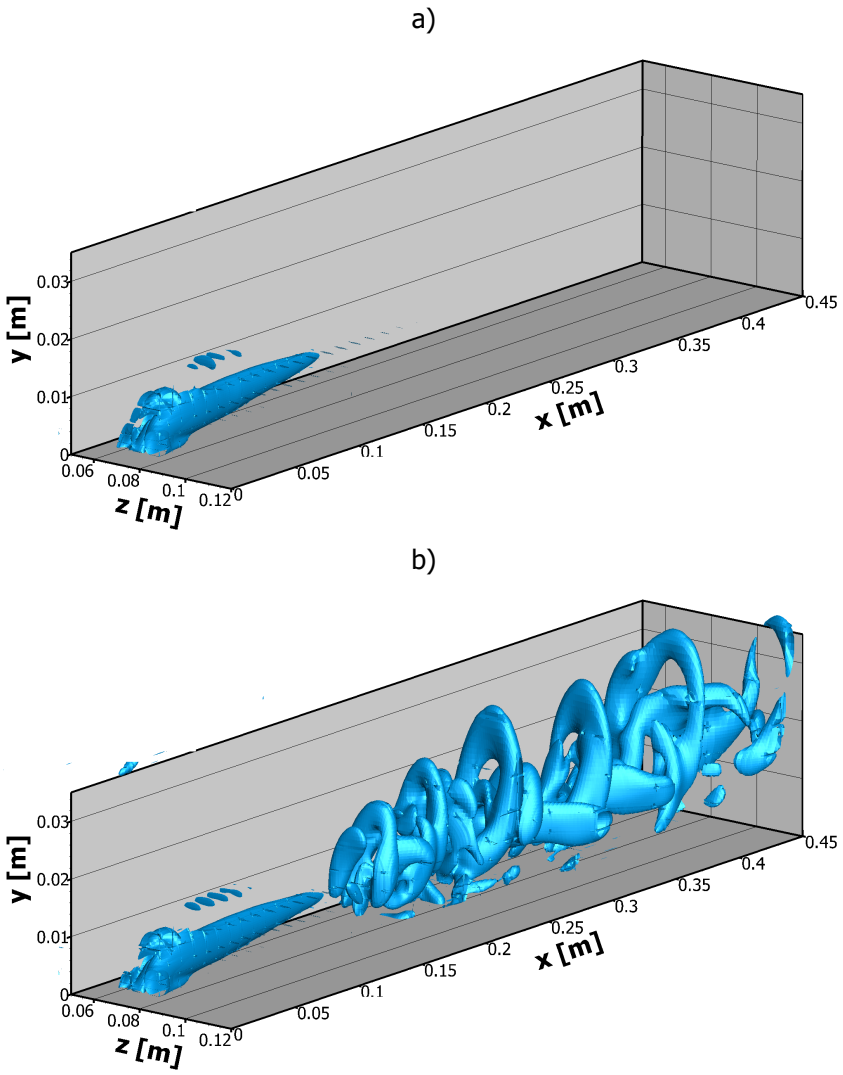

Fig 7. Isosurface contour of Q-crtierium $Q = 5.5 \cdot 10^7$ of the steady (a) and unsteady (b) cross-flow vortex

development of the steady (a) and unsteady (b) vortex downstream of the wake for patch 2. The highly accelerated flow favours stabilisation and damping of the vortex. The perturbation induces a finger-like structures at x=0.16 m at the downstream tip of the cross-flow-like vortex. Further downstream, horse-shoe vortices are observed. A similar observation is made for the other roughness configurations and a similar configuration by Di Giovanni and Stemmer [11].
The unsteady results are analysed with a temporal and a spatio-temporal Fourier transformation. Different modes of the streamwise velocity are investigated with the temporal Fourier transformation. The spatio-temporal Fourier transformation of a generic flow variable $q(x,y,z,t)$ is defined as

$$Q_{m,n}(x,y) = \sum_{j=0}^{J-1} \sum_{l=0}^{L-1} q(x,y,z_j,t_l) e^{-i2\pi(nj/J+ml/L)}, \tag{17}$$

where J is indicating the number of samples in spanwise direction and L is referring to the number of time steps. The multiples of the fundamental frequency are indicated by m and the multiples of the spanwise wave length by index n.
The local maximum in the wall-normal direction (y) describes the amplitude of the mode (m,n) for a

Table 2. Streamwise vorticity magnitudes of random roughness patches

Patch Number	ω_x
1	172,797.29 [1/s]
2	213,554.17 [1/s]
3	229,972.87 [1/s]

given location in x. The amplitude $A^q_{m,n}$ is given by

$$A^q_{m,n}(x) = \max_{y \geq 0} \left| Q_{m,n(x,y)} \right| . \tag{18}$$

A Fourier transformation is performed on the streamwise velocity values. The Fourier amplitudes û are normalised with the boundary-layer edge velocity u_{edge}=1600 m/s at the inflow. In Fig. 8, the logarithmic value of this normalised Fourier amplitudes are plotted. At first, we study the downstream development of the the perturbation frequency f_1=8.3 kHz and wavenumber n=1 in Fig. 8a. The amplitudes are damped until x=0.14 m for patch 2 and x=0.2 m for patch 1 and 3. Further downstream, the Fourier amplitudes rise linearly until a certain location where an exponential increase in magnitude is observed for all three patches. The development is similar for all patches, but the location of the jump is occurring at different downstream locations. The beginning of the finger-like structures is corresponding to the sudden rise in the Fourier amplitudes and is taken as the transition location in this study.
The influence of different wavenumbers and frequencies is presented in Fig. 8b for patch 3, but a similar development is also observed for patch 1 and 2. In the plot, the harmonics (f_2,f_3) of the perturbation frequency f_1 also have a reduced amplitude compared to f_1. For higher harmonics (not shown), the amplitude is reduced further but behaves similarly. Upstream the transition region the wavenumber n=3 is larger than the rest of the amplitudes for all frequencies. The spanwise wavenumber n=3 corresponds to the wavelength of the vortex. After the exponential increase in amplitudes, a similar behaviour is seen for all wavenumbers.

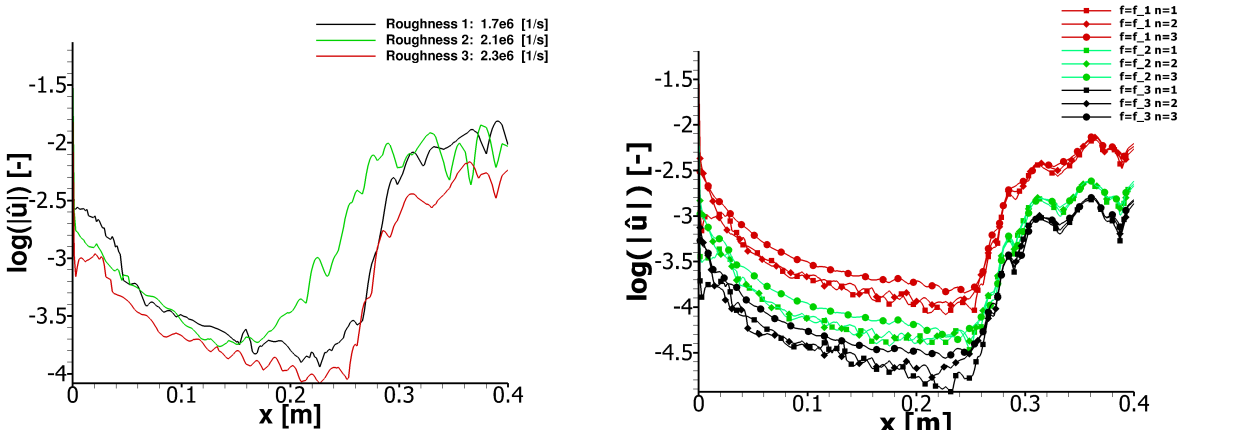

(a) $f = f_1$,$n = 1$ for patch 1,2 and 3 (b) different frequencies and wavenumbers for patch 3

Fig 8. Normalised maximum amplitudes for temporal and spatial Fouriermodes

Finally, we see in Fig. 9 how the maximum streamwise vorticity and the wall-normal location of the vortex core at the inflow is influencing the transition location for the three different roughness patches. We defined the transition location as the beginning of the jump in Fourier amplitudes of the perturbation frequency in this study. We observe, that for larger values of this value the transition location is further upstream. A quadratic relation between the maximum streamwise vorticity times the vortex core location and the transition location is observed. Higher vorticity itself does not necessarily lead

to transition further upstream and faster perturbation growth. A vortex located further away from the wall is transporting low-momentum fluid in faster regions of the boundary layer more effectively. This generates strong gradients in the shear-flow where the unsteady perturbations grow, as observed in [4].

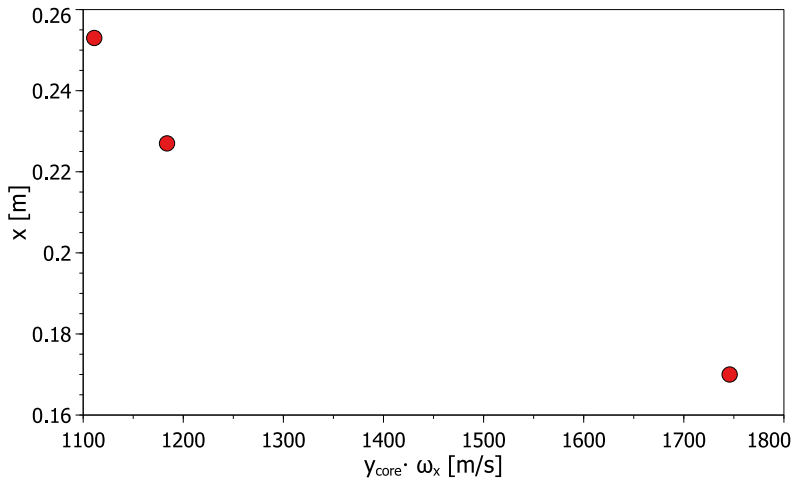

Fig 9. Relation between maximum streamwise vorticity and transition position

7. Conclusion and summary

This study investigated cross-flow-like vortices in the wake of random distributed roughness patches. In the steady base-flow, a cross-flow vortex is formed in the wake downstream the highest peak within the roughness patch.
Since the vorticity magnitude has a direct influence on transition, a database of 9180 DNS simulation was computed and was utilised for machine-learning driven vorticity prediction. Two different network types were used in this investigation: A DNN type network used input parameters derived from the surface geometry. An average error in the predictions of 17% was achieved for the DNN. A better prediction was shown by the CNN. The method is using an image of the roughness surface as input to predict the vorticity with an average error of only 13%. Hence, ML methods can provide a fast possibility to estimate the streamwise vorticity in the wake and provide information on stability.
In order to investigate the connection between vorticity magnitude and transition location, the steady vortex in the wake is disturbed in unsteady simulations by a pressure, velocity, density and temperature wave. These disturbances are amplified in the shear flow of the vortex and lead to transition. Finger-like structures are rising at the tip of the steady vortex. We studied three different patches with a low, medium and high streamwise vorticity in the wake. For all patches, a sudden jump occurs in the Fourier modes of the streamwise velocity. For stronger vorticity magnitudes of the cross-flow vortex, we do not observe transition further downstream in every case, although the flow-field is more disturbed by the stronger vortex. A relation for the streamwise vorticity and the transition location can be formulated by considering the product of the wall-location and the streamwise vorticity of the cross-flow-type vortex. This study showed a framework for a possible transition prediction criterion in the future. However, further studies need to investigate the influence of a noisy disturbance signal including several frequencies on different cross-flow-like vortices. Also the influence of geometric roughness parameter on the formation of the streamwise vorticity needs to be investigated in the future.

Acknowledgements

This research was supported by founds of the TUM International Graduate School of Science and Engineering (IGSSE) and the Cusanuswerk e.V scholarship. Further, the authors gratefully acknowledge

the Gauss Centre for Supercomputing e.V. (www.gauss-centre.eu) for supporting this project by providing computing time on the GCS Supercomputer SuperMUC-NG at Leibniz Supercomputing Centre (www.lrz.de).

References

1. Schneider, S.P.: Summary of hypersonic boundary-layer transition experiments on blunt bodies with roughness. Journal of Spacecraft and Rockets 45, 1090–1105 (2008)
2. Van den Eynde, J.P., Sandham, N.D.: Numerical simulations of transition due to isolated roughness elements at mach 6. AIAA Journal 54, 53–65 (2016)
3. Di Giovanni, A., Stemmer, C.: Roughness-induced crossflow-type instabilities in a hypersonic capsule boundary layer including nonequilibrium. Journal of Spacecraft and Rockets 56, 1409–1423 (2019)
4. Ulrich, F., Stemmer, C.: Investigation of vortical structures in the wake of pseudo-random roughness surfaces in hypersonic reacting boundary-layer flows. International Journal of Heat and Fluid Flow 95, 108945 (2022)
5. Brunton, S.L., Noack, B.R., Koumoutsakos, P.: Machine learning for fluid mechanics. Annual Review of Fluid Mechanics 52, 477–508 (2020)
6. Aghaei Jouybari, M., Yuan, J., Brereton, G.J., Murillo, M. S.: Data-driven prediction of the equivalent sand-grain height in rough-wall turbulent flows. Journal of Fluid Mechanics 912, A8 (2021)
7. Park, C.: A review of reaction rates in high temperature air. In 24th Thermophysics Conference. AIAA paper 89 - 1740 (1989)
8. Blottner, F.G., Johnson, M., Ellis, M.: Chemically reacting viscous flow program for multicomponent gas mixtures. Technical report, Sandia Labs., Albuquerque, N. Mex. (1971)
9. Hirschfelder,J.O., Curtiss,C.F., Bird,R.B.: University of Wisconsin. Theoretical Chemistry Laboratory. Molecular theory of gases and liquids. Structure of matter series. Wiley, New York (1954)
10. Wilke, C.R.: A viscosity equation for gas mixtures. The Journal of Chemical Physics 18(4), 517–519 (1950)
11. Di Giovanni, A., Stemmer, C.: Cross-flow-type breakdown induced by distributed roughness in the boundary layer of a hypersonic capsule configuration. Journal of Fluid Mechanics 856, 470–503 (2018)
12. Baum, M., Poinsot, T., Thévenin,D.: Accurate boundary conditions for multicomponent reactive flows. Journal of Computational Physics 116(2), 247 – 261 (1995)